

# Conformationally regulated “nanozyme-like” cerium oxide with multiple free radical scavenging activities for osteoimmunology modulation and vascularized osseointegration

Shusen Bao<sup>a,c,1</sup>, Dongmei Yu<sup>a,b,1</sup>, Zhen Tang<sup>a,1</sup>, Hao Wu<sup>a</sup>, Hao Zhang<sup>d</sup>, Ning Wang<sup>a</sup>, Yichao Liu<sup>a</sup>, Hai Huang<sup>a</sup>, Chaozong Liu<sup>b,\*\*</sup>, Xiaokang Li<sup>a,\*\*\*</sup>, Zheng Guo<sup>a,\*</sup>

<sup>a</sup> Department of Orthopedics, Tangdu Hospital, Fourth Military Medical University, Xi'an, 710038, China

<sup>b</sup> University College London, UCL Institute of Orthopaedics and Musculo-Skeletal Science, M14 the Royal National Orthopaedic Hospital, Stanmore, HA7 4LP, United Kingdom

<sup>c</sup> Department of Orthopedics, No. 903 Hospital of PLA Joint Logistic Support Force, Hangzhou, 310000, China

<sup>d</sup> Department of Burn Surgery, Xijing Hospital, Fourth Military Medical University, Xi'an, 710038, China

## ARTICLE INFO

### Keywords:

Nanozyme-like” cerium oxide  
Durable redox activation  
Free radical scavenging  
Osteoimmunology modulation  
Vascularized osseointegration

## ABSTRACT

Given post-operative aseptic loosening in orthopedic disease treatment, osteointegration occurs at the bone-implant interface as a holistic process, including immunoregulation (e.g., macrophage polarization), angiogenesis and osteogenesis in sequence. In order to achieve early rapid and satisfactory osseointegration, different nano-shaped (nanocone, nanopolyhedron and nanoflower abbr. NC, NP & NF) cerium oxide (CeO<sub>2-x</sub>) coatings, endowed with “nanozyme-like” activities for multiple free radical elimination and osteoimmunology regulation, were hydrothermally synthesized on titanium alloy (TC4). *In vitro* cell experiments showed that nano-CeO<sub>2-x</sub> coated TC4 not only induced polarization of RAW264.7 cells toward M2 phenotype, but also promoted angiogenesis and vascularization of endothelial cells along with differentiation and mineralization of osteogenic precursor cells. Improvements in M2-polarized macrophage, angiogenesis, and bone regeneration were further confirmed in a rat femoral condyle model. Among the above three nano-morphologies, NF exhibited the best osseointegration. RNA sequencing and mechanism exploration suggested that the inhibition of PI3K-AKT signaling pathway was essential for immunomodulatory capacity of NF. In conclusion, it provided promising insights into the immunomodulatory exploitation of orthopedic implants.

## 1. Introduction

Arthroplasty has become a proven therapeutic alternative for severe osteoarthritis with increasing popularity [1,2]. More than one million total hip replacements were annually performed worldwide [3]. In the United States over 370,000 total hip replacements were initially conducted in 2014, while in the United Kingdom 97,000 cases were undertaken in 2017, and additionally the number of global hip/knee replacements was ever-increasing [4,5]. Although implant survival rates achieve stable growth, patients were still subjected to the risk of surgical

revision. In England and Wales, data collected from 1 million hip replacements by the National Joint Registry (NJR) revealed that post-operative revision primarily resulted from aseptic loosening of the implant (accounting for 48% of all cases [4]), attributing to poor osseointegration at the bone-implant contact interface [6]. Osteointegration, a temporal process occurring at the bone-implant interface, involves immunoregulation, vascularization of endothelial cells, osteogenic differentiation and mineralization of osteogenic precursor cells [7–9]. It was reported that bone immunomodulation, the early inflammatory response of immune cells (e.g., neutrophils, lymphocytes, and

Peer review under responsibility of KeAi Communications Co., Ltd.

\* Corresponding author.

\*\* Corresponding author.

\*\*\* Corresponding author.

E-mail addresses: [chaozong.liu@ucl.ac.uk](mailto:chaozong.liu@ucl.ac.uk) (C. Liu), [lxfmmu@163.com](mailto:lxfmmu@163.com) (X. Li), [guozheng@fmmu.edu.cn](mailto:guozheng@fmmu.edu.cn) (Z. Guo).

<sup>1</sup> Co-first authors: These authors contributed equally to this work.

<https://doi.org/10.1016/j.bioactmat.2023.12.006>

Received 7 October 2023; Received in revised form 20 November 2023; Accepted 5 December 2023

2452-199X/© 2023 The Authors. Publishing services by Elsevier B.V. on behalf of KeAi Communications Co. Ltd. This is an open access article under the CC BY-NC-ND license (<http://creativecommons.org/licenses/by-nc-nd/4.0/>).

macrophages) mediated by graft surface physicochemical characteristics (including nano-topography and chemical substance, such as free radicals), determined the fate of implanted graft [10,11]. Once biomaterials of bone repair implanted *in vivo*, macrophages, as one of the important effector cells involved in bone immunomodulation, can be polarized to either M1 (pro-inflammatory) or M2 (anti-inflammatory) phenotype in stimulation of physicochemical characteristics on biomaterial surface [12,13]. However, M1 macrophages incurred amplification and delay of the inflammatory response with high reactive oxygen species (ROS) characteristic, osteoclastic behavior and inhibition of osteogenesis by up-regulating the expression and secretion of some pro-inflammatory factors (e.g., TNF- $\alpha$ , IL-6, IL-1, etc.) [13–15]. Moreover, M1 macrophages induced excessive release of endogenous free radical-typed nitric oxide in the progression of inflammatory response in which L-arginine was oxidized to citrulline to produce NO on account of inducible nitric oxide synthase (iNOS) catalysis. Proinflammatory cytokines activated iNOS to overproduce NO, which in turn induced damage at the site of inflammation [16]. Therefore, one of the important anti-inflammatory strategies was removal of ROS and NO overproduction. On the contrary, M2 macrophages secreted large amounts of anti-inflammatory factors (e.g. IL-10 and TGF- $\beta$ , etc.) as well as angiogenic and osteogenic growth factors (VEGF, PDGF-BB and BMP-2, etc.) contributing to new bone formation [10,17]. Advances in materials biology manifested that the surface physicochemical properties (such as surface morphology, chemical composition and hydrophilicity, etc.) of biomaterials mediated a cascade reaction of cellular behaviors and mutual interaction, from their bioactivity to functional expression [18,19]. Therefore, it is extremely desirable to realize biomaterial-modulated osseointegration via early pro-healing immunoregulation, succedent angiogenesis and osteogenesis, thereby reducing the risk of post-surgically aseptic loosening.

Recently, cerium oxide has been paid a widespread attention due to its multiple enzymatic activities, especially its capability to scavenge free radicals [20–22]. Numerous researches have demonstrated that cerium oxide nanoparticles (CeONPs) were possessed with the potential to reduce inflammation response, and promote osteoblastic cell functionalization and new bone formation [21,23,24], on account of their auto-redox degree conferred by the coexistence and interconversion of Ce<sup>4+</sup> and Ce<sup>3+</sup> oxidation states for free radical scavenging. In the physiological environment, superoxide dismutase of Ce<sup>3+</sup> state and catalase mimetic activities of Ce<sup>4+</sup> state have been verified to be capable of scavenging superoxide (O<sub>2</sub><sup>-</sup>) and hydrogen peroxide (H<sub>2</sub>O<sub>2</sub>), respectively [25–27]. As a reactive oxygen species scavenger in the inflammatory microenvironment, CeONPs downregulated inflammatory factor release and thus inhibited the inflammatory response via inhibitory MAPK-NF $\kappa$ B signaling pathway, thereby promoting the repair of damaged tissues. CeONPs with different Ce<sup>4+</sup>/Ce<sup>3+</sup> ratios by magnetron sputtered on titanium surface effectively facilitated M2 phenotypic switch of macrophages and osteogenic differentiation of mesenchymal stem cell (MSCs), thus accelerating early osseointegration [24]. It is noted that different shaped-CeONPs coated on titanium (Ti) surface, enhanced antibacterial and anti-inflammatory functions around implants [27]. In addition, CeONPs with fewer Ce<sup>3+</sup> valence content has been proved to perform better free radical scavenging capability of nitric oxide [28].

Nevertheless, different nano-morphologic cerium oxide coatings via hydrothermal deposition remained relatively scarce, and the mechanisms of their immunomodulation and osteoinductive actions deserved to be elucidated further. Titanium-based implants due to excellent biocompatibility and mechanical properties, were widely applied as clinical bone repair or substitute materials, but their bioactivities in terms of osseointegration at bone-implant interface remained deficient [29]. Hence, a surface-functionalized titanium implant endowed with bioactivities was requested to be capable of mediating cell behavior, and thereby accelerating bone regeneration during postoperative healing phase. Herein, different nano-shaped cerium oxide coatings

hydrothermally deposited on the surface of titanium alloys were prepared to imitate nanozyme biofunction for multiple free radical scavenging. Effect of different nanomorphologies of “nanozyme-like” cerium oxide (nano-CeO<sub>2-x</sub>) associated with their auto-redox action on macrophage polarization orientation and resulting immune microenvironment was investigated, which determined the vascularized osseointegration. It revealed the mechanism of nano-shaped cerium oxide-mediated biochemical factors for osteoimmunology modulation, providing a promising insight into design of implant biofunction to achieve early osseointegration.

Schematic. Mechanism of action of “nano-enzymatic” cerium oxide preparation, Osteoimmunology Modulation and Vascularized Osseointegration.

## 2. Experimental methods

### 2.1. Fabrication of nano-CeO<sub>2-x</sub> coated macro/micro roughed titanium alloy

Machined titanium alloy (TC4: Ti6Al4V) discs ( $\varnothing$ 14 × 2 mm) and screws (M1.6 × 4 mm) were sandblasted treatment to obtain macro roughed surface with high-speed alumina (Al<sub>2</sub>O<sub>3</sub>) sand grains using sandblasting machine (9070A, Xi'an quailed Tongchuang Machinery Co., Ltd., China). For macro/micro roughed surface, the aforementioned titanium alloy plates and screws with macro roughed surface were etched by mixed acid solution (HCl: HF: H<sub>2</sub>O = 5%: 10%: 85% (volume ratio)) for 1 min. Thereafter, titanium alloy discs and screws with macro/micro roughed surface soaked in mixed solution of 0.434g/10 mL Ce (NO<sub>3</sub>)<sub>3</sub>·6H<sub>2</sub>O and 1.2g/40 mL urea were respectively subjected to hydrothermal treatment at 120 °C, 180 °C, 210 °C for 4 h to acquire corresponding nano-flower, nano-cone and nano-polyhedron (abbr. NF, NC and NP) shaped cerium oxide coatings.

### 2.2. Structural characterization of nano-CeO<sub>2-x</sub> coated macro/micro roughed titanium alloy

The morphology of nano-CeO<sub>2-x</sub> coated macro/micro roughed titanium alloy surface was observed using a scanning electron microscope (SEM, SU6600, Japan) equipped with energy dispersive spectrometer (EDS). Phase identification of nano-CeO<sub>2-x</sub> coated TC4 represented by NF, was conducted by a thin film X-ray diffractometer (TF-XRD; XPert Pro, Netherland). Nano-CeO<sub>2-x</sub> scratched from the coatings were examined with a transmission electron microscope (TEM; JEOL-JEM 2100 F, Japan) and TEM-equipped EDX (JEOL, Japan). The element composition and chemical bonds of nano-CeO<sub>2-x</sub> were identified using an X-ray photoelectron spectroscopy (XPS; Thermo Scientific ESCALAB Xi+, USA) with C1s peak at binding energy of 284.6 eV for calibration. The surface roughness of nano-CeO<sub>2-x</sub> coated macro/micro roughed titanium alloy surface were detected using a laser scanning confocal microscope (LSCM; KEYENCE VK-X1000, Japan) on microscale and an atomic force microscope (AFM; BRUKER Dimension Icon, Germany) on nanoscale. The hydrophilicity was measured using a contact angle device (DSA30, Kruss, Germany) with a 2  $\mu$ L droplet of distilled water applied to a disc for triplicate.

ROS scavenging capacity: The total ROS scavenging capacity of nano-CeO<sub>2-x</sub> coatings was detected by Total Antioxidant Capacity Assay Kit with FRAP method (S0116, Beyotime, China). Briefly, nano-CeO<sub>2-x</sub> was scraped from corresponding coating surface and dispersed in distilled water to attain the detecting solution containing nano-CeO<sub>2-x</sub> of 0.1 M concentration. The total antioxidant capacity of nano-CeO<sub>2-x</sub> was assessed by taking 5  $\mu$ L of the detecting solution in 180  $\mu$ L of FRAP working solution and incubating at 37 °C for 5 min, followed by absorbance measurement of blue Fe<sup>2+</sup>-tripyridyltriazine at 593 nm. The catalase (CAT) activity of nano-CeO<sub>2-x</sub> was determined by Catalase Assay Kit (S0051, Beyotime, China). Four microliters of the detecting solution were added to 200  $\mu$ L of chromogenic work solution before

incubation at 25 °C for 30 min, and the absorbance of chromogenic substrate colorated red by the oxidation of hydrogen peroxide was measured at 520 nm. Total Superoxide Dismutase Assay Kit with WST-8 (S0101, Beyotime, China) was used to assay superoxide dismutase (SOD) activity of the detecting solution. According to the manufacturer's instructions, the SOD enzyme activity was quantified by incubating the detecting solution with the working solution for absorbance measure at 450 nm. Nano-CeO<sub>2-x</sub> capability of scavenging ROS and RNS was quantified by chromogenic reaction using a reactive oxygen species kit (S0033S, Beyotime, China) and a NO detection kit (S0019, Beyotime, China), respectively.

### 2.3. Cell culture

Murine-derived macrophage cell line (RAW264.7), human umbilical vein endothelial cells (HUVECs), and mouse-derived osteogenic precursor cell line (MC3T3-E1) provided by the Chinese Academy of Sciences were used in following research. RAW264.7 cells were cultured in 1640 medium (RPMI-1640; Gibco, USA) containing granulocyte-macrophage colony-stimulating factor (Peprotech, USA). HUVECs in DMEM high-glucose medium (DMEM; Gibco, USA), and MC3T3-E1 cells in Minimum Essential Medium  $\alpha$  ( $\alpha$ -MEM; Gibco, USA) were cultured. Both 10 % fetal bovine serum (FBS; Gibco, USA) and 1 % penicillin/streptomycin (Gibco, U.S.A.) were supplemented in the above basal culture medium respectively for cell incubation in atmosphere of 5 % CO<sub>2</sub> and 95 % humidity at 37 °C. After 3 d of incubation, the culture medium from RAW264.7 cells on bare and nano-CeO<sub>2-x</sub> coated TC4 discs were respectively collected and mixed with the DMEM or MEM complete medium at a ratio of 1:1 to obtain conditioned media (CM), namely CM-DMEM or CM-MEM.

### 2.4. Immunoregulatory evaluation of RAW264.7 cells on bare and nano-CeO<sub>2-x</sub> coated TC4 discs

RAW264.7 cells at a density of  $2 \times 10^4$  cells per well, were seeded on bare and nano-CeO<sub>2-x</sub> coated TC4 discs centrally placed in 24-well tissue culture plates (TCP) for predetermined culture time. After 1 d of incubation, the cells were fixed with 4 % paraformaldehyde, dehydrated and sprayed with gold for cell morphology observation by scanning electron microscopy (SEM, SU6600, Japan). ROS and RNS scavenging capability of RAW264.7 cells on bare and nano-CeO<sub>2-x</sub> coated TC4 for 48 h incubation were respectively visualized with 0.1 % V/V DCFH-DA and DAF-FM-DA for observation by fluorescence microscope (CX21, Olympus, Japan), and the average fluorescence intensity of captured images were analyzed with Image J software.

The immunofluorescent staining of iNOS and CD206 proteins in RAW264.7 cells on bare and nano-CeO<sub>2-x</sub> coated TC4 discs was used to evaluate inflammatory response. After incubation of 3 days, RAW264.7 cells were fixed with 4 % paraformaldehyde for 20 min at 4 °C, permeabilized with 0.1 % Triton X-100 for 10 min and then blocked with 5 % bovine serum albumin (BSA) for 1 h. Whereafter, RAW264.7 cells were incubated with rabbit anti-mouse primary antibody against inducible nitric oxide synthase (iNOS) at a dilution ratio of 200 and sheep anti-mouse primary antibody against cluster of differentiation 206 (CD206) at a dilution ratio of 300 at 4 °C overnight. iNOS marker was fluorescently labeled in red and CD206 marker in green visualized with donkey anti-rabbit and donkey anti-goat IgG antibodies at a dilution ratio of 200 (BIOSS, China) respectively, while cell nuclei were labeled in blue by 4,6-diamidino-2-phenylindole (DAPI; ServiceBio, China). The immunofluorescent staining images of RAW264.7 cells were captured using a laser scanning confocal microscope (LSCM; FV1200, Olympus, Japan).

Furthermore, the secretion levels of tumor necrosis factor  $\alpha$  (TNF- $\alpha$ ) and interleukin-10 (IL-10) at 3 and 7 d, along with platelet-derived growth factor-BB (PDGF-BB) and bone morphogenetic protein 2 (BMP2) at 7 d by RAW264.7 cells on bare and nano-CeO<sub>2-x</sub> coated TC4

discs were determined using the corresponding enzyme-linked immunosorbent assay kits (ELISA; Thermo Fisher Scientific, U.S.A.). mRNA expression of CC-chemokine receptor-7 (CCR-7) and arginase-1 (Arg-1) in RAW264.7 cells at 3 days was detected by real-time quantitative polymerase chain reaction (RT-qPCR; LightCycler@96, Roche, Switzerland). In briefly, total cellular RNA was isolated with Trizol reagent (Invitrogen, USA) and then converted to cDNA with a reverse transcription kit (Takara, Japan), followed by mixing with SYBR Green Mastermix (Transgen, Biotech, China) and primers to quantify the expression levels of related genes. The expression levels of target genes relative to glyceraldehyde-3-phosphate dehydrogenase (GAPDH) as an endogenous reference gene, were normalized by the 2<sup>- $\Delta\Delta$ CT</sup> method. The primer sequences of the genes tested in this research were exhibited in Table S1. RAW264.7 cells were grown for 3 days under NF stimulation and one group was treated with 740Y-P activator. Fluorescent staining for iNOS and CD206 protein, as well as mRNA expression of CCR-7 and Arg-1 were performed.

### 2.5. Angiogenic capability of HUVECs stimulated by bare and nano-CeO<sub>2-x</sub> coated TC4 discs

The migration capability of HUVECs was evaluated by Transwell invasion assay and scratch assay. HUVECs on bare and nano-CeO<sub>2-x</sub> coated TC4 discs (directly stimulated by samples: DSS) and in CM respectively incubated for 5 days, were resuspended in serum-free medium and seeded at a density of  $2 \times 10^4$  cells per mL in the top chamber with 8  $\mu$ m pore sized permeable membrane. Hereafter, HUVEC medium containing 10 % FBS was added in the bottom chamber of 24-well plates. After 24 h of incubation, HUVECs on top surface of the permeable membrane were wiped with a wet cotton swab, while the counterpart ones migrated to the bottom of permeable membrane were fixed with 4 % paraformaldehyde for 20 min and then stained with crystal violet staining solution (C0121, Beyotime, China) for photograph using a light microscope (CX21, Olympus, Japan). HUVECs migrated across permeable membrane were counted using Image J soft. Furthermore, HUVECs in the modes of DSS and CM for 5 d incubation were respectively reseeded in 6-well plates at a density of  $5 \times 10^5$  cells per mL, and then HUVECs were scratched perpendicular to the well plates using a 20  $\mu$ L pipette after they just reached complete monolayer confluence. The scratch images at 0 and 12 h of incubation after scratch were photographed with a microscope (CX21, Olympus, Japan). HUVECs migration length was measured using Image J software.

Angiogenic capacity of HUVECs was evaluated by tubule formation assay. Matrigel (BD Biosciences, USA) was thawed overnight at 4 °C and spread in 96-well plates and solidified at 37 °C for 30 min. HUVECs from DSS and CM of 5 d incubation were respectively reseeded at a density of  $2 \times 10^4$  cells per well in 96-well plates containing Matrigel. HUVECs cultured for 12 h were photographed by light microscope (CX21, Olympus, Japan). The number of branch points and the total capillary tube length as indicators of angiogenic capacity were measured.

Moreover, the vascular subtypes of HUVECs, characterized by cluster of differentiation (CD31) and endomucin (Emcn), were identified using immunofluorescence staining. After incubation of 5 days, HUVECs in DSS and CM pattern were fixed with 4 % paraformaldehyde for 20 min, permeabilized with 0.1 % Triton X-100 for 10 min and then blocked with 5 % BSA for 1 h. Thereafter, HUVECs were then incubated overnight at 4 °C with 1:100 dilutions of anti-CD31 (ABCAM; AB24590) and Emcn (affinity; DF13357) antibodies. CD31 marker in red and Emcn marker in green were fluorescently labeled with goat anti-rabbit and goat anti-mouse IgG antibodies (BIOSS, China) at a dilution ratio of 200 respectively, while nuclei were stained with DAPI. Fluorescent images were captured by fluorescence microscope (CX21, Olympus, Japan).

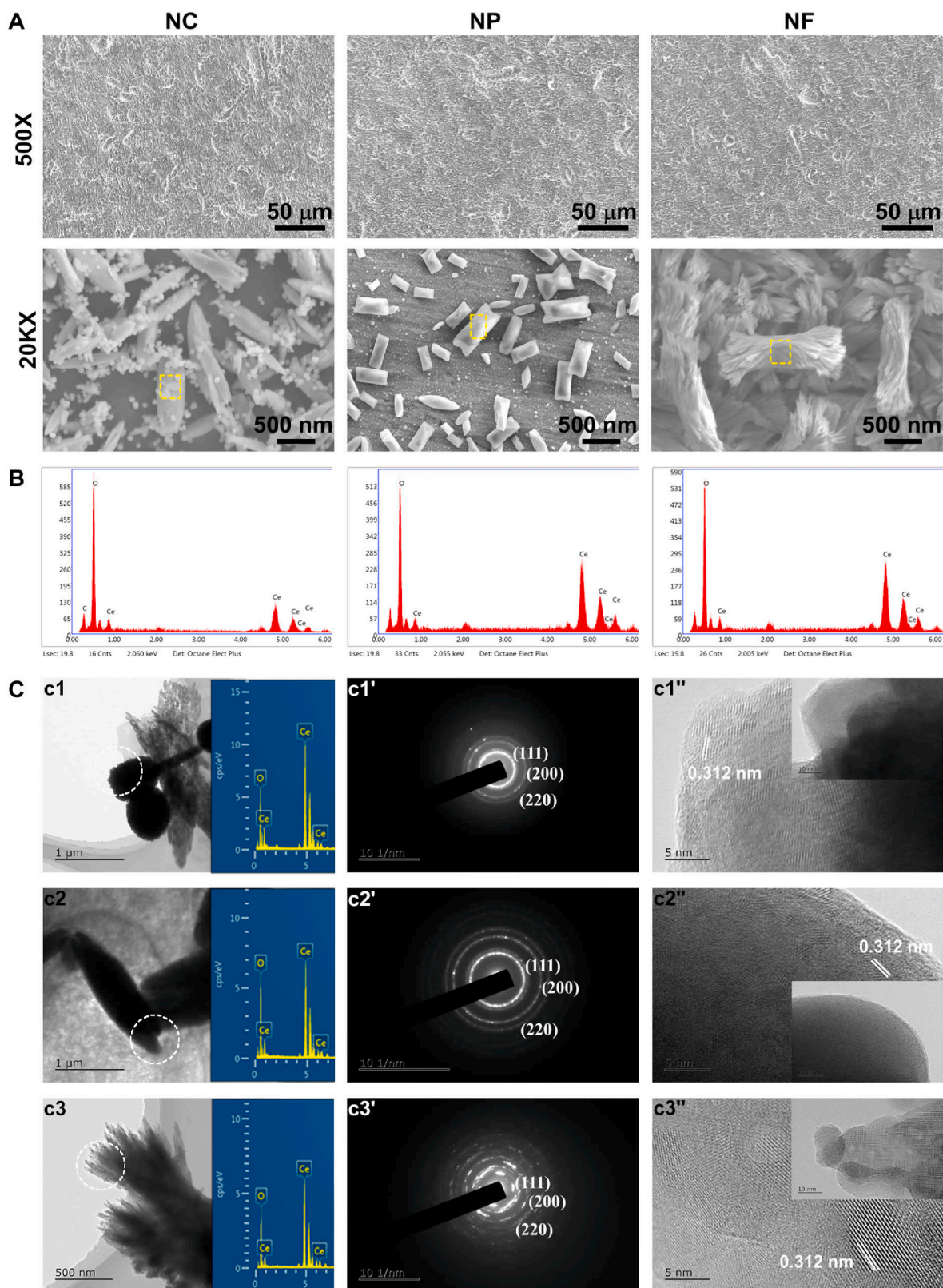


**Fig. 1.** Structural characterization of NC, NP and NF- shaped cerium oxide coated macro/micro roughed titanium alloy (TC4). (A) Low and high magnified SEM images. (B) EDS spectrum of yellow marked zones in (A). (C) TEM images of NC, NP and NF- shaped cerium oxide scratched from corresponding coatings, comprising bright field images, inserted EDX spectra, SAED patterns and HRTEM images.

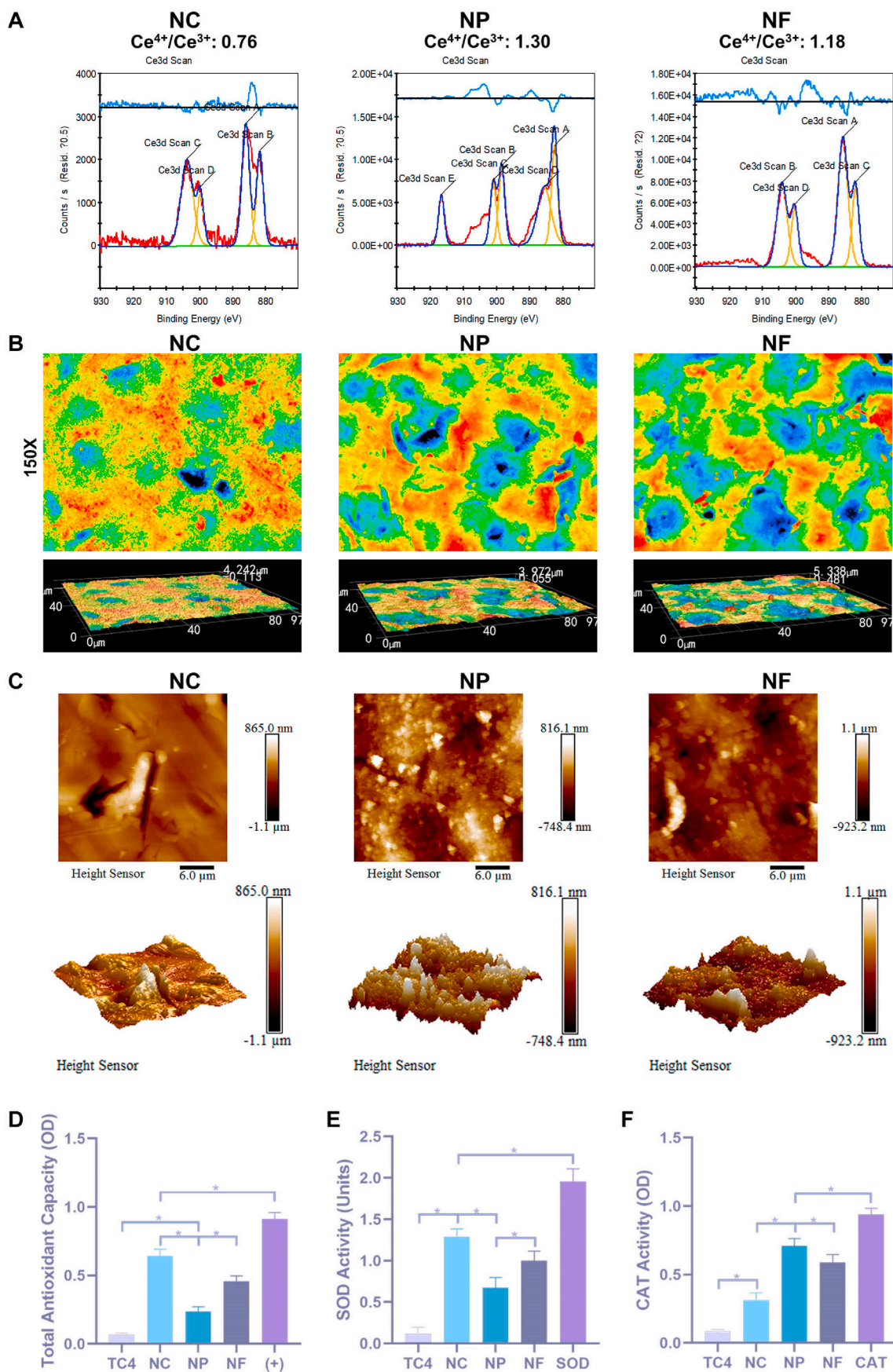


Fig. 2. (A) XPS peak-differentiating of Ce 3d, (B) LSCM images, (C) AFM images, (D) Total antioxidant capacity, (E) SOD activity and (F) CAT activity of NC, NP and NF- shaped cerium oxide coatings (+: positive control). \*p < 0.05.

## 2.6. Osteogenic evaluation of MC3T3-E1 cells on bare and nano-CeO<sub>2-x</sub> coated TC4 discs

Cell proliferation of MC3T3-E1 cells seeded on bare and nano-CeO<sub>2-x</sub> coated TC4 discs for incubation of 24, 48 and 72 h was evaluated using Cell Counting Kit-8 (CCK-8, C0038, Beyotime, China). In brief, MC3T3-E1 cells at a density of 10<sup>4</sup> cells per mL were seeded on bare and nano-CeO<sub>2-x</sub> coated TC4 in 24-well plates and then cultured for 24, 48 and 72 h. 100 mL CCK-8 reagent were added in each well and incubated at 37 °C for 1 h. Absorbance values of medium supernatant were measured at 450 nm absorbance. In addition, MC3T3-E1 cells incubated for 72 h were fixed with 4 % paraformaldehyde for 20 min and then stained using FAK100 kit (Abcam, USA) for cytoskeleton observation, followed by photography using a fluorescence microscope (CX21, Olympus, Japan).

Alkaline phosphatase (ALP) and alizarin red staining were used to evaluate the osteogenic differentiation and mineralization of MC3T3-E1 cells. MC3T3-E1 cells in the mode of DSS and CM respectively cultured for 48 h were digested with pancreatic enzymes and then reseeded at a density of 2 × 10<sup>4</sup> cells per mL in 24-well plates for incubation of pre-determined time. Alkaline phosphatase (ALP) staining at 7 and 14 days and alizarin red staining at 21 days of MC3T3-E1 cells were performed. Briefly, MC3T3-E1 cells were fixed with 4 % paraformaldehyde, and stained with ALP and alizarin red staining kit (Servicebio, China), followed by photograph with microscope (CX21, Olympus, Japan).

## 2.7. RNA sequencing (RNA-seq) analysis and western blotting verification

RAW264.7 cells seeded on bare and NF-coated TC4 discs were collected after incubation of 3 days and total RNA was respectively extracted using TRIZOL reagent (Invitrogen, Carlsbad, CA, USA). mRNA enrichment, lysis, reverse transcription, library construction and HiSeq X Ten analyses were carried out by Shanghai Energy Biotech Co. Ltd. The threshold for differentially expressed transcripts (DETs) was P < 0.05 and an absolute fold change of ≥2. Function and signaling pathway enrichment analyses of DETs were performed using Gene Ontology (GO) and Kyoto Encyclopedia of Genes and Genomes (KEGG) databases. Differences between bare and NF coated TC4 in predefined genomes were analyzed using GSEA (v4.1.0).

Furthermore, RNA-seq analysis was verified by western blotting (WB). Briefly, RAW264.7 cells cultured on bare and NF-coated TC4 discs for 3 d were respectively lysed with radioimmunoprecipitation assay (RIPA) lysis buffer (Fdbio science, China) containing protease and phosphatase inhibitors (ThermoFisher Scientific, USA), followed by centrifugation and supernatant collection. For the above each group, 30 µg corresponding protein was isolated by sodium dodecyl sulfate polyacrylamide gel electrophoresis (SDS-PAGE) and transferred to a polyvinylidene fluoride (PVDF) membrane (Merck Millipore, MA, USA). The protein-transferred membranes were blocked and incubated with primary antibodies against PI3K, phospho-PI3K, AKT, phospho-AKT, and β-actin overnight at 4 °C, followed by the addition of horseradish peroxidase (HRP)-coupled secondary antibodies. Finally, the aforementioned membranes were pictured using an enhanced chemiluminescence (ECL) kit (Millipore, USA) and a chemiluminescence imaging system. Grey scale values in the WB bands were quantified using Image J software.

## 2.8. Osteoimmunomodulation of bare and nano-CeO<sub>2-x</sub> coated TC4 screws implanted in rat femoral condyles

Surgical procedures on experimental animals were approved by the Institutional Laboratory Animal Centre and the Ethics Committee of the Fourth Military Medical University. Sixty-four SD rats (male, ~200 g/each rat) at eight weeks of age were randomly divided into four groups (16 in each group) for implantation. The rats were anaesthetized by

intraperitoneal injection of 20 mg of sodium pentobarbital solution. Screws were implanted in both hind limb femoral condyles of a rat (one screw per femoral condyle) after drilling a hole of  $\varnothing 1.5 \times 4$  mm at each femoral condyle, followed by suturing layer by layer. Penicillin was injected intramuscularly for 3 days after surgery to prevent from infection. The postoperative rats were executed with overdose an aesthesia at 1, 2, 4 and 6 w respectively. The femoral condyles containing screws were acquired and subsequently applied to evaluate new bone formation around the implanted screws using Micro-CT (AX-2000; Always Imaging, China) at source voltage of 150 kV, beam current of 160 µA and scanning resolution of 15 µm, and 3D reconstruction using AYRecon software. Based on the obtained scanning data, 3D bone reconstruction around implanted screws and their quantization were conducted with VG Studio MAX software. For histological examination, screw-contained femoral condyles were fixed with 4 % paraformaldehyde, dehydrated in 95 % ethanol, embedded with polymethylmethacrylate (PMMA), cut into 150 µm thick sections using an interlocked diamond saw (Leitz 1600, Germany) and then polished to 20 µm thick slices for Van Gieson (VG) staining and microscopical observation. In addition, screw-free femoral condyles were fixed with 4 % paraformaldehyde, decalcified in 10 % EDTA solution, dehydrated in gradient ethanol, embedded into paraffin and sectioned into 5 µm thin sections with a cutting-unit (Leica, Germany) for Masson staining, cluster of differentiation 86(CD86)/CD206 and CD31/Emcn fluorescence staining, respectively. The frozen screw-removed femoral condyles were sliced into the section with thickness of 5 µm for fluorescent probe loading using Reactive oxygen species kit (S0033S, Beyotime, CN). The Total Nitric Oxide Assay Kit (MX4732, Beyotime, CN) was used to quantify the level of total nitric oxide in the surrounding tissue of screws after homogenization. The staining images were captured using a panoramic scanner (250/MIDI, Hungary) for quantitative evaluation using Image J software.

## 2.9. Statistical analysis

All experiments were performed at least 3 independent replications, analyzed with SPSS 19.0 software and expressed as mean ± standard deviation (SD). Statistical analyses were performed using one-way analysis of variance (ANOVA) and Student-Newman-Keuls (SNK) post hoc test, where \*P < 0.05 was determined as significant difference.

## 3. Result and discussion

### 3.1. Structural characterization of nano-CeO<sub>2-x</sub> coated TC4

Low and high magnified SEM images of nano-CeO<sub>2-x</sub> coatings, represented by NC, NP and NF, hydrothermally deposited on sandblasting and acid etching incurred macro/micro roughed titanium alloy surface were shown (Fig. 1A). It indicated that the hydrothermal temperature can effectively regulate the nanomorphology of CeO<sub>2-x</sub> coatings, and the lower temperature promoted the nano-CeO<sub>2-x</sub> coatings with higher specific surface area, which may also be conducive to macrophage towards M2 polarization and osteoblast functions [27]. EDS spectrum (Fig. 1B) and XRD pattern (Fig. S1 (Supplementary Information, SI)) of NF as a representative of nano-CeO<sub>2-x</sub> coatings revealed that nano-CeO<sub>2-x</sub> coatings contained Ce and O elements, and their phase compositions were composed of CeO<sub>2-x</sub>. In addition, TEM bright-field images, SAED patterns and HRTEM images of NC, NP and NF-shaped cerium oxide taken from corresponding nano-CeO<sub>2-x</sub> coatings further confirmed that nano-morphologic cerium oxide coatings are of polycrystallized CeO<sub>2-x</sub> as determined by the SAED patterns, HRTEM images and inserted EDX spectra (Fig. 1C). Ratios of Ce<sup>4+</sup> and Ce<sup>3+</sup> (Ce<sup>4+</sup>/Ce<sup>3+</sup>) of NC, NP and NF-shaped CeO<sub>2-x</sub> coatings were in sequence of NC (0.76) < NF (1.18) < NP (1.30) as identified by high-resolution XPS spectrum of Ce 3d (Fig. 2A). NC, NP and NF-shaped CeO<sub>2-x</sub> coatings exhibited similar microscale roughness as revealed by LSCM (Fig. 2B), while nanoscale

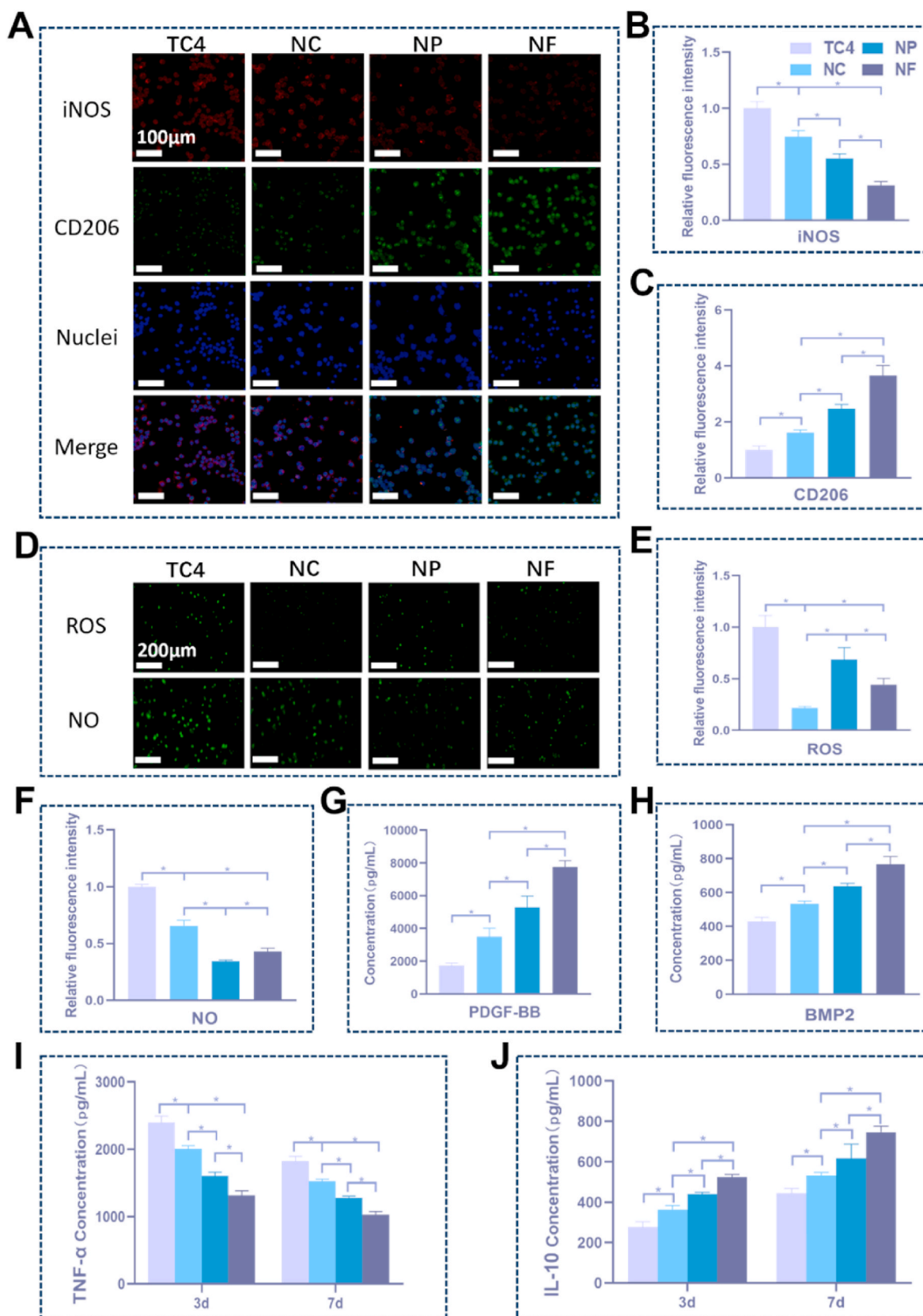


**Fig. 3.** Phenotypic polarization and free radical scavenging capacity of RAW264.7 cells on TC4, NC, NP, and NF: (A) Fluorescence images of iNOS (red), CD206 (green) and nuclei (labeled as blue) in RAW264.7 cells at day 3 of incubation along with (B) iNOS and (C) CD206 relative fluorescence intensity. (D) Fluorescence images of ROS and NO in RAW264.7 cells at 48 h of incubation together with (E) ROS and (F) NO relative fluorescence intensity. The concentration of (G) PDGF-BB and (H) BMP2 at 3 days, as well as (I) TNF- $\alpha$  and (J) IL-10 at 3 and 7 days secreted by RAW264.7 cells. \* $p < 0.05$ .

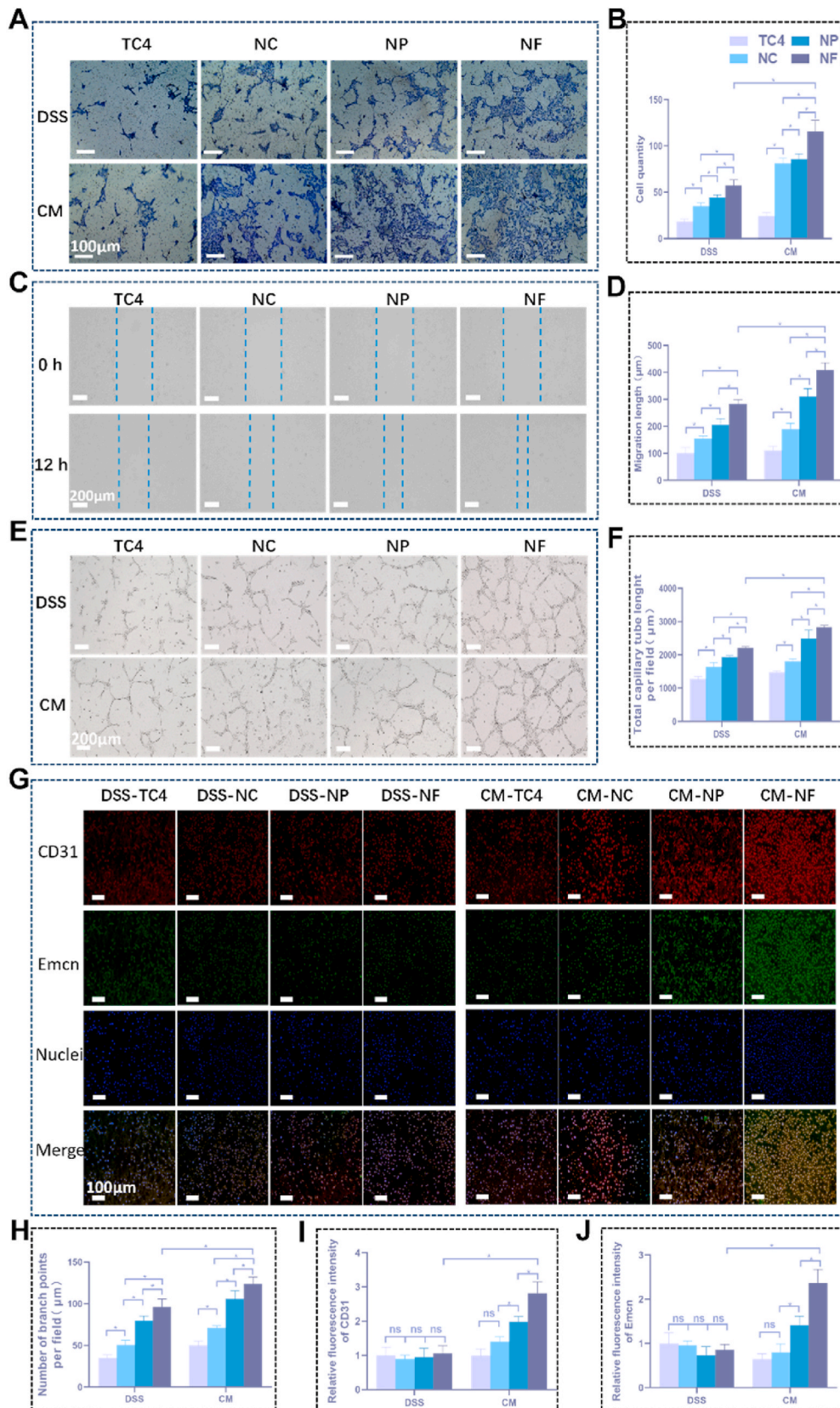


**Fig. 4.** Angiogenesis of HUVECs in pattern of DSS and CM, respectively. (A) Crystal violet staining images and (B) counting of the invasive HUVECs on Transwell membrane at 24 h. (C) Scratch images at 0 and 12 h and (D) quantified migration length of HUVECs. (E) Vessel tube formation images of HUVECs along with (F) total capillary length and (H) number of branch points per field at 12 h. (G) Fluorescence staining images and relative intensities of (I) CD31 (red) and (J) Emcn (green) in HUVECs at 5 d \**p* < 0.05.

roughness value of NF-shaped CeO<sub>2-x</sub> coatings was slightly higher than those of NC and NP counterparts as verified by AFM (Fig. 2C), indicating that NF was possessed with higher specific surface area. Contact angles of water droplets on NC, NP and NF coatings were similar but lower than that of bare TC4, suggesting that NC, NP and NF-shaped CeO<sub>2-x</sub> coatings due to their chemical composition and nanotopography, significantly improve the hydrophilicity of TC4 (Fig. S2 (SI)).

### 3.2. Free radical scavenging capability of bare and nano-CeO<sub>2-x</sub> coated TC4

During the osteointegration process, sustained excess of oxygen and nitrogen radicals incurred oxidative stress and intensively prolonged the inflammatory period, thereby inhibiting osteogenesis [25,26,30]. Meanwhile, it was generally assumed that the removal of ROS and RNS facilitated macrophage polarization to M2 phenotype conducive to osseointegration [25–27,31,32]. Induction of interconversion between Ce<sup>3+</sup> and Ce<sup>4+</sup> states exhibited similar superoxide dismutase (SOD) antioxidant and catalase (CAT) activities to catalyze reactions with superoxide and hydrogen peroxide, along with nitric oxide radical scavenging ability to inhibit inflammatory mediator production and protect cells from oxidative stress damage [22,25,28]. SOD prevented 2-(2-Methoxy-4-nitrophenyl)-3-(4-nitrophenyl)-5-(2,4-disulphophenyl)-2H-tetrazole monosodium salt (WST-8) and xanthine oxidase from catalyzing the production of formazan dye, and therefore the yield of formazan dye negatively correlated with SOD activity. Compared with TC4, the enhanced antioxidant capacity of nano-CeO<sub>2-x</sub> coatings were exhibited (Fig. 2D–F). It was noted that the antioxidant capacity of NC was higher than that of the other coatings in this work as certified by total antioxidant capacity and SOD activity, while the CAT activity trended in the order of NP > NF > NC. In summary, nano-CeO<sub>2-x</sub> coatings exhibited excellent antioxidant capacity, and the differences between the groups may be related to the different Ce<sup>4+</sup>/Ce<sup>3+</sup> ratios in CeONPs [28,33].

### 3.3. Polarization behavior of RAW264.7 cells on bare and nano-CeO<sub>2-x</sub> coated TC4

The morphologies of RAW264.7 cells adhering to bare and nano-CeO<sub>2-x</sub> coated TC4 discs for 3d were shown (Fig. S4 (SI)). RAW264.7 cells on TC4 were spherical with no obvious pseudopods, while the counterparts on nano-CeO<sub>2-x</sub> coated TC4 were prolonged and exhibited obvious filamentous pseudopods, and the effect of NF on RAW264.7 cells was more evident. In conclusion, it indicated that nano-shaped cerium oxide coatings significantly promoted RAW264.7 cells adhesion and spread. It was reported that macrophage morphology might be closely related to their polarization phenotype, in which rounded macrophages were typical M1 phenotype, whereas M2 phenotypic macrophages tended to be spindle-shaped with elongated filamentous pseudopods [34].

The immunomodulatory effects of nano-CeO<sub>2-x</sub> coatings on polarization tendency of highly plastic RAW264.7 cells were explored by immunofluorescent staining and cytokine secretion. Immunofluorescent staining images of iNOS and CD206 along with their quantitative analyses revealed that nano-CeO<sub>2-x</sub> coatings prominently enhanced the protein expression of CD206 marked M2, but decreased the protein expression of iNOS marked M1 (Fig. 3A–C), suggesting that nano-shaped CeO<sub>2-x</sub> coatings, in particular NF, were inclined to present anti-inflammatory effect characterized by M2 polarized RAW264.7 cells. The secretion levels of inflammation-related cytokines from RAW264.7 cells on bare and nano-CeO<sub>2-x</sub> coated TC4 discs, such as pro-inflammatory TNF-α and anti-inflammatory IL10, appeared the anti-inflammatory trend similar to that of immunofluorescent staining (Fig. 3G and H). Furthermore, nano-shaped CeO<sub>2-x</sub> coatings, especially NF, facilitated the secretion of pro-angiogenic PDGF-BB and pro-osteogenic BMP2 cytokines compared to TC4 (Fig. 3I and J). In

summary, nano-CeO<sub>2-x</sub> coatings accelerated the polarization of adherent RAW264.7 cells toward M2 state compared to TC4, resulting in up-regulated expression and secretion of anti-inflammatory cytokine as well as pro-angiogenic and pro-osteogenic cytokine secretion with NF performing the most pronounced efficacy.

To uncover the underlying regulatory mechanisms of nano-CeO<sub>2-x</sub> induced RAW264.7 cells, intracellular ROS and NO scavenging of RAW264.7 cells on bare and nano-CeO<sub>2-x</sub> coated TC4 discs were detected. In accord with the trend of anti-inflammatory effect, the ROS and NO scavenging capacities of nano-CeO<sub>2-x</sub> coatings against RAW264.7 cells were significantly higher than those of TC4, while NF displayed complementary excellence both ROS and NO scavenging capacities as verified by intracellular ROS and NO staining images (Fig. 3D–F). Excessive ROS induced high oxidative stress levels, resulting in severer inflammatory response as well as cellular damage and even apoptosis [26]. L-arginine was oxidized to citrulline concurrently producing NO for iNOS catalysis. Meanwhile, pro-inflammatory cytokines activated iNOS to overproduce NO, which in turn incurred inflammatory injury [31]. To sum up, complementary efficiency both ROS and RNS scavenging activities of NF possibly contributed to M2 polarization of RAW264.7 cells.

### 3.4. Angiogenesis of HUVECs in response to nano-CeO<sub>2-x</sub> and cytokines secreted from RAW264.7 cells

Blood vessels were in charge of transporting cells, nutrients, and waste products intimately related to early osteogenesis [35]. The migration capability of HUVECs in mode of DSS and CM detected by Transwell invasion assay and scratch assay, revealed that nano-CeO<sub>2-x</sub> exhibited a stronger capability to promote HUVECs migration than TC4 as a control (Fig. 4A–D, and Fig. S5 (SI)). Thereinto, HUVECs in CM mode showed a more pronounced migration trend than those in DSS mode. It might largely attribute to anti-inflammatory cytokines and pro-angiogenic growth factors secreted from M2 phenotypic RAW264.7 cells on bare and nano-CeO<sub>2-x</sub> coated TC4 discs. Notably, the capability of NF to promote HUVECs migration was the strongest in DSS and CM patterns. To observe the angiogenic capacity of HUVECs, capillary tube formation assay was performed. Representative angiogenesis images and quantitative analyses (Fig. 4E) displayed the trends similar to those of migration. CeONPs was demonstrated to increase vessel density and angiogenesis via promoting the proliferation and migration of vascular endothelial cells, which might ascribe to the antioxidant effect of CeONPs protecting local lipid and protein from oxidation [36].

To explore the antioxidant and immunoregulatory effect of nano-shaped CeO<sub>2-x</sub> coatings on angiogenesis, fluorescence staining of CD31 and Emcn marked blood vessel in HUVECs was performed. The protein expression level of CD31 and Emcn in HUVECs in pattern of DSS and CM was ranked in the order of NF > NP > NC > TC4, while their expression levels in CM mode were higher than corresponding those in DSS pattern (Fig. 4G). H typed blood vessel characterized by high expression of CD31 and Emcn (CD31<sup>hi</sup> and Emcn<sup>hi</sup>) could promote local vascular growth and provide ecological niche signaling for perivascular bone progenitor cells through the enhancement of HIF and Notch signaling pathways [26]. Therefore, the abundance of CD31<sup>hi</sup> and Emcn<sup>hi</sup> in endothelial cells as an indicator of vessel sub-type, was generally applied to determine the vascular growth status conducive to osteogenic function.

On one hand, HUVECs themselves could secrete both pro-angiogenic (e.g. PDGF-BB) and pro-osteogenic (e.g. BMP2) cytokines conducive to osteogenic behavior of MC3T3-E1 [37,38]. On the other hand, anti-inflammatory and pro-angiogenic cytokine secreted in CM by RAW264.7 cells significantly contributed to the angiogenic behavior of HUVECs, which further enhanced osteogenic function of MC3T3-E1 [37,39,40]. RAW264.7 cells of M2 phenotype contributed to assembling of type-H capillaries via secreting PDGF-BB, which could recruit osteocytes and osteoblasts for sequent osteoblastic differentiation during bone modeling and remodeling [41,42]. Furthermore, more and more new

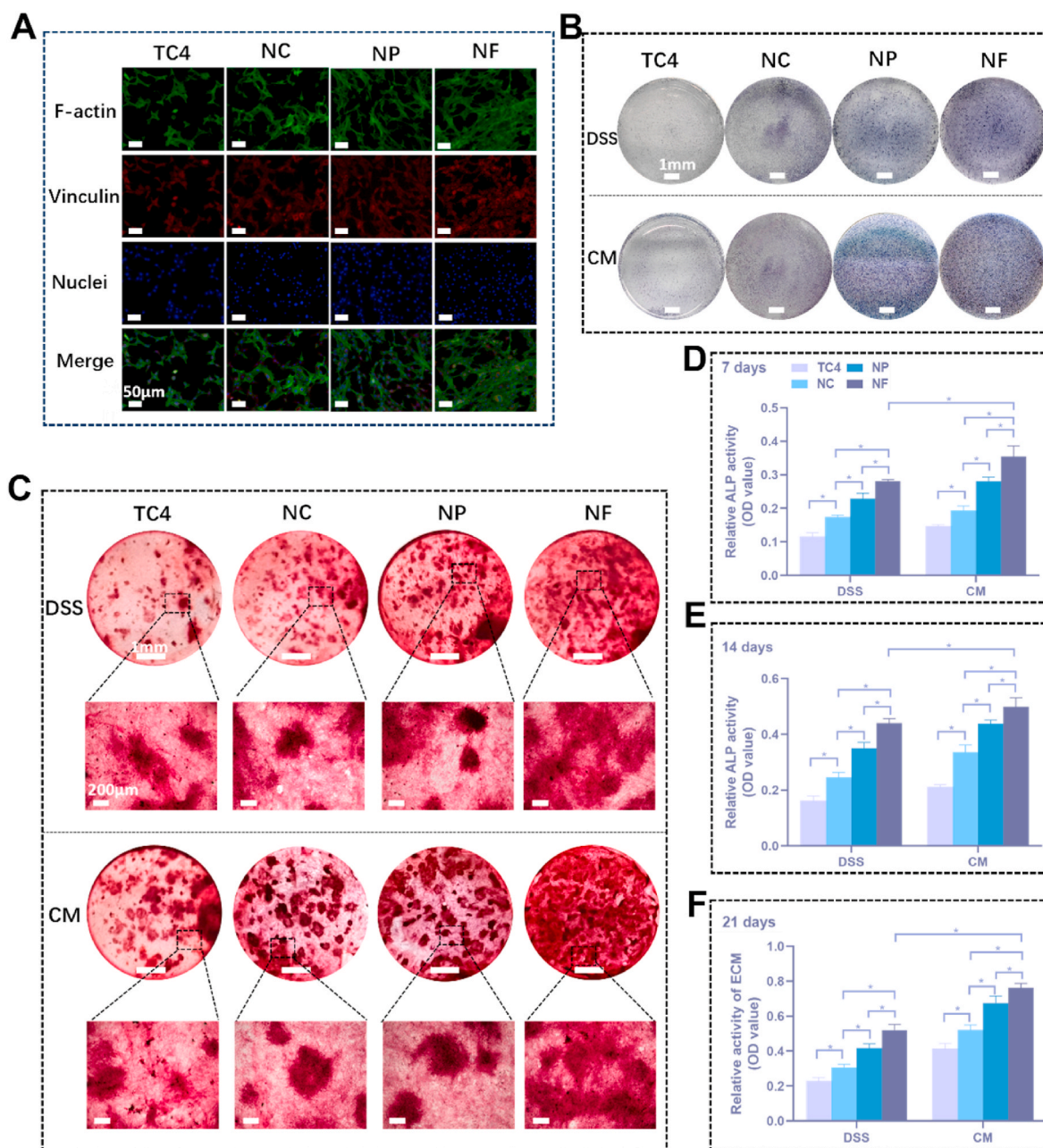


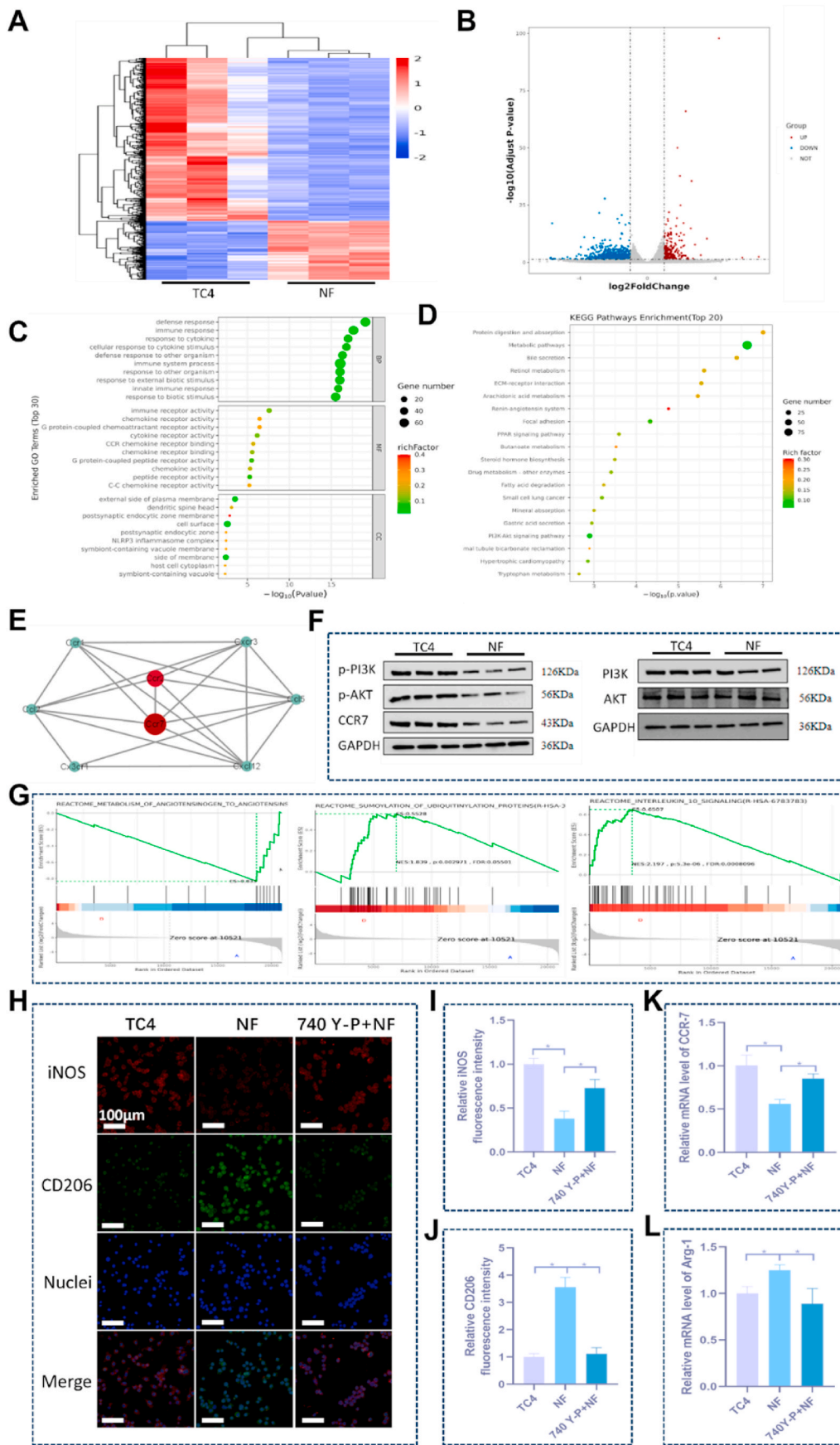
**Fig. 5.** Adhesion, osteogenic differentiation and mineralization of MC3T3-E1 cells: (A) Fluorescent staining of F-actin (green), vinculin (red), and nuclei (blue) in MC3T3-E cells at 3 d of DSS mode. (B) Representative ALP staining images of MC3T3-E cells at 14 d and (C) Alizarin Red staining images of mineralized nodules in MC3T3-E cells at 21 d co-cultivated in DSS and CM respectively. (D, E) Quantized ALP activity at 7 and 14 d, and (F) mineralized nodule quantification at 21 d \* $p < 0.05$ .

blood vessels generated by HUVECs in stimulation of RAW264.7 cell CM could transport abundant cells, oxygen and nutriment required for bone regeneration. In sum, angiogenic capacity of HUVECs in pattern of CM was further enhanced compared with that in DSS mode, resulting from the secretion of pro-angiogenic growth factors by RAW264.7 cells on nano-CeO<sub>2-x</sub> coatings, especially on NF with complementary efficiency for both ROS and RNS scavenging activities.

### 3.5. Osteogenesis of MC3T3-E1 in response to nano-CeO<sub>2-x</sub> and cytokines secreted from RAW264.7 cells

Cell morphology visualized by cytoskeleton fluorescence staining and proliferation of MC3T3-E1 seeded on bare and nano-CeO<sub>2-x</sub> coated TC4 discs indicated that nano-CeO<sub>2-x</sub> coatings promoted cell adhesion,

spread and proliferation compared to TC4 as a control (Fig. 5A). CCK-8 assayed viability of MC3T3-E1 on TC4, NC, NP and NF revealed that the cells proliferated with prolonging incubation time, while no significance on each group at 24 h, noticeable significance was observed on NF relative to others at 48 h and the trend of NF > NP > NC > TC4 was exhibited at 72 h (Fig. S6 (SI)). Osteogenic differentiation and mineralization respectively verified by ALP staining and its activity quantification as well as extracellular matrix (ECM) mineralization and its quantitative analysis of MC3T3-E1 in DSS and CM patterns were performed. It indicated that MC3T3-E1 in pattern of CM displayed higher ALP activity and ECM mineralization indicative of osteogenesis than those in DSS mode, in which nano-CeO<sub>2-x</sub> coatings, in specific NF, exhibited notable efficacy relative to TC4 (Fig. 5B–F and Fig. S7 (SI)). Ce<sup>4+</sup> was considered to directly enhance osteogenesis by promoting



(caption on next page)

**Fig. 6.** RNA-seq analysis of RAW264.7 cells cultured for 3 days on NF and TC4 as a control along with certification for inhibition of inflammatory response. (A) Volcano plot, (B) heatmap diagram, (C) GO pathway enrichment and (D) KEGG enrichment of differentially expressed genes. (E) PPI network analysis of the differential-regulated pathways. (F) Representative western blots of inflammation-associated signaling pathways in RAW264.7 cells. (G) Enrichment analysis of regulated gene pathways using KEGG and genome database. (H–J) Representative iNOS (red)/CD206(green) immunofluorescence images and their relative fluorescence intensities, along with (K) CCR-7 and (L) Arg-1 mRNA expression in RAW264.7 cells with and without 740 Y–P treatment on NF and TC4 as a control. \* $p < 0.05$ .

cellular adhesion, proliferation and osteogenic differentiation of osteoblasts as well as mineral deposition [24].

However, higher  $Ce^{4+}/Ce^{3+}$  ratio in cerium oxide nanoparticles was more favorable for new bone formation and bone-implant integration. Different nano-shaped  $CeO_{2-x}$  coatings exhibited osteogenic function of MC3T3-E1 in the sequence of NF > NP > NC > TC4, concurrently considering nano-topography with high specific surface area and appropriate valence ratio of  $Ce^{4+}$  and  $Ce^{3+}$  for NF. In contrast, NF with relatively excellent osteogenic function had a  $Ce^{4+}/Ce^{3+}$  ratio of 1.18 closer to 1, meaning that proportions of  $Ce^{4+}$  and  $Ce^{3+}$  were almost approximate and  $Ce^{4+}$  proportion was slightly more, which possibly contributed to interconversion activation of both.

### 3.6. RNA-seq analysis and verification of free radical scavenging of nano- $CeO_{2-x}$ coatings against inflammatory responses

It was tentatively inferred that nano- $CeO_{2-x}$  coatings were possessed with nano-enzymatic activity for multiple free radical scavenging and achieved osteoimmunology modulation and vascularized osseointegration, with NF being of the strongest efficacy. To explore this biologically underlying mechanism, RNA-sequence of RAW264.7 cells on bare and NF coated TC4 discs was detected to analyze their differences in transcript levels. The clustering heatmap and volcano plot of their differential gene expression revealed that the up-regulated genes (such as IL-1b, CCL22, USP18, etc.) were associated with M2 phenotype of macrophages, while the down-regulated genes (such as Atf3, HIF-1a, Yap1, etc.) were related to M1 phenotype of macrophages (Fig. 6A–B). Gene ontology (GO) terminology indicated that the effect of NF on the biological processes, cellular components, and molecular functions of RAW264.7 cells mainly focused on protein binding, signal transduction, and nuclear gene transcription, suggesting that NF modulated RAW264.7 cells polarization by promoting cell adhesion and subsequent nuclear transcription. Furthermore, analysis of the top 20 enriched pathways using Kyoto Encyclopedia of Genes and Genomes (KEGG) data revealed that immunoregulation-related pathways, including PPAR and PI3k-AKT signaling pathway, were highly enriched (Fig. 6C–E). These functional annotations suggested that NF facilitated macrophages toward M2 polarization by inhibiting the PI3K- AKT signaling axis.

Genomic enrichment analysis (GSEA) showed a decrease in the expression of genes associated with the pro-inflammatory response and an increase in the expression of genes associated with anti-inflammation in RAW 264.7 cells on NF relative to those in RAW264.7 cells on TC4 as a control (Fig. 6G). To elucidate how these pathways were regulated under NF activation, western blotting of the major protein kinases and phosphorylation levels regarding PI3K-AKT signaling pathway (PI3K, AKT), as well as CCR7 was performed (Fig. 6F). Li et al. revealed that the low surface potential of Ti surface could generate repulsion of bone marrow-derived monocytes (BMDMs) and activate anti-inflammatory M2 polarization of macrophages, thereby promoting bone regeneration through the secretion of osteoclastogenic factors, in which inhibition of the PI3K-Akt-mTOR signaling axis was key to its immunomodulatory capacity [11]. Yan et al. explained that nintedanib could inhibit the protein expression of M1 polarized macrophage marker through the MAPK/PI3K- AKT pathway, consequently inhibiting synovial inflammation and fibrosis and reducing articular cartilage degeneration [43]. In our work, nano- $CeO_{2-x}$  coatings could induce M2 switch of macrophages by eliminating ROS and RNS, for PI3K-AKT pathway inhibition critical for their function.

It further confirmed the down-regulation of the protein expression of p-PI3K, p-AKT, and CCR7 in RAW264.7 cells on NF compared to that in RAW264.7 cells on TC4. To verify the role of PI3K- AKT signaling axis in macrophage polarization mediated by synergetic clearance of ROS and RNS, iNOS and CD206 protein levels in RAW264.7 cells on NF treated with and without 740 Y–P (a cell-permeable PI3K activator [44]) were examined. Compared with 740 Y–P -untreated RAW264.7 cells, up-regulated iNOS and down-regulated CD206 expressions were perceived in RAW264.7 cells treated with 740 Y–P, which were comparable to those in RAW264.7 cells on TC4, while mRNA expression of CCR-7 and Arg-1 showed similar results (Fig. 6H–L).

### 3.7. Inflammation, angiogenesis and osteogenesis in tissue around bare and nano- $CeO_{2-x}$ coated TC4 screws in rat femoral condyles

Inflammation at 1 week and angiogenesis at 2 weeks after implantation in tissue around bare and nano- $CeO_{2-x}$  coated TC4 screws in rat femoral condyles were visualized by immunofluorescence staining (Fig. 7). At 1 week after surgery, ROS and NO levels in tissue around nano- $CeO_{2-x}$ -coated screws were significantly lower than those in tissue around TC4 screw (Fig. 7A, E). Moreover, macrophages recruited around nano- $CeO_{2-x}$  coated TC4 screws were of significant M2 phenotypic polarization, as proved by downregulated CD86 and upregulated CD206 expressions (Fig. 7B, F, G). Thereinto, NF manifested the most prominent efficacy. Remarkable CD31<sup>hi</sup> and Emcn<sup>hi</sup> expressions of endothelial cells were observed around nano- $CeO_{2-x}$  coated TC4 screws at 2 weeks after operation (Fig. 7C, H, I). It suggested that nano- $CeO_{2-x}$  coatings, especially NF, significantly promoted H-typed angiogenesis conducive to subsequent osteogenesis.

Micro-CT reconstruction after different implantation times confirmed that newly formed bone quantified by bone volume fraction (BV/TV), trabecular number (Tb.N), and trabecular thickness (Tb.Th) was notably more around nano- $CeO_{2-x}$  coated screws compared with that around TC4 screw, with the order of NF > NP > NC > TC4 (Fig. 8A, D–F). Histological identification around bare and nano- $CeO_{2-x}$  coated TC4 screws at the postsurgical week of 1, 2, 4 and 6 was detected to further evaluate osteointegration around screws implanted in rat femoral condyles. After 1 and 2 weeks of implantation, Masson staining images showed a small amount of collagen around the TC4 screws, whereas abundant collagen appeared around the nano- $CeO_{2-x}$  coated screws, with the increasing trend of NF > NP > NC (Fig. 8B, G). After 4 weeks after implantation, a small amount of mature bone appeared around TC4 screw as demonstrated by VG staining images, while continuous mature bone emerged around nano- $CeO_{2-x}$  coated screws, with the bone amount in trend of NF > NP > NC (Fig. 8C, H, I). Meanwhile, the collagen fibers around the nano- $CeO_{2-x}$  coated TC4 screws (especially NF) were more regular and compact, largely ensuring early mechanical bearing and interfacial osteointegration between new bone and screws. The amount of newly formed bone around screws further increased pronouncedly as the postoperative time extended to 6 weeks, with the trend of peripheral bone formation amount in accord with the postoperative time. In summary, nano- $CeO_{2-x}$  coatings, in specific NF, boosted early osteogenesis and interfacial osteointegration in comparison to bare TC4 screw. Red lines indicative of new bone (labeled with alizarin red) and green lines indicative of new bone (labeled with calcein) were observed within the bone tissue surrounding the screw (Fig. S8 (SI)), and the average width of the gap between the red and green lines was calculated to determine the mineralized attachment rate (MAR) values. At 6 weeks, nano- $CeO_{2-x}$

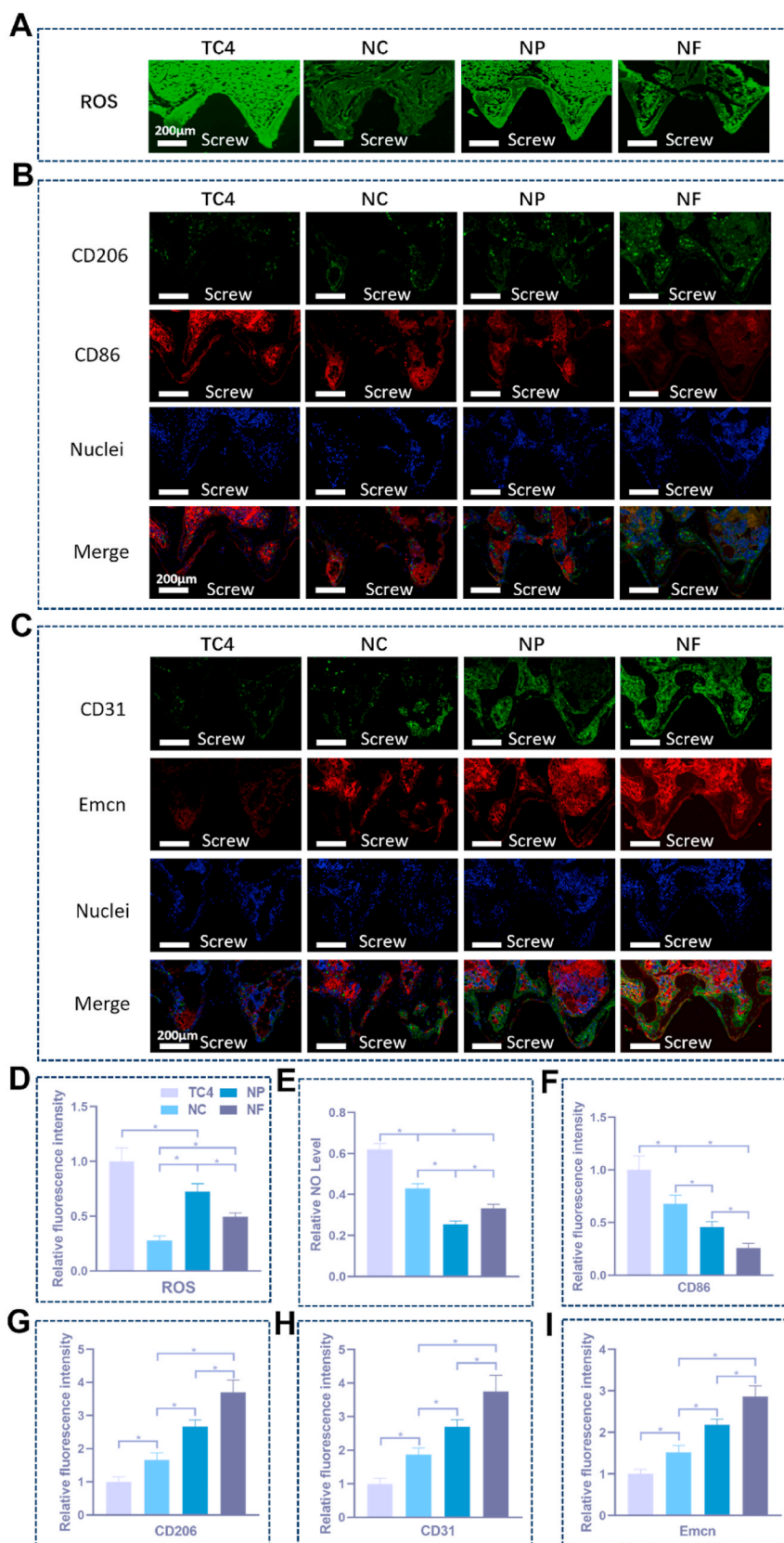


**Fig. 7.** Fluorescence staining images of tissue around implanted screws in rat femoral condyles: Fluorescence staining images of (A) ROS, (B) CD86 (red), CD206 (green) and nuclei (blue) at 1 week of implantation, together with (C) CD31 (green), Emcn (red) and nuclei (blue) at 2 weeks of implantation. (D) Relative fluorescence intensity of ROS and (E) NO level. Statistically relative fluorescence intensity of (F) CD86, (G) CD206, (H) CD31 and (I) Emcn. \* $p < 0.05$ .

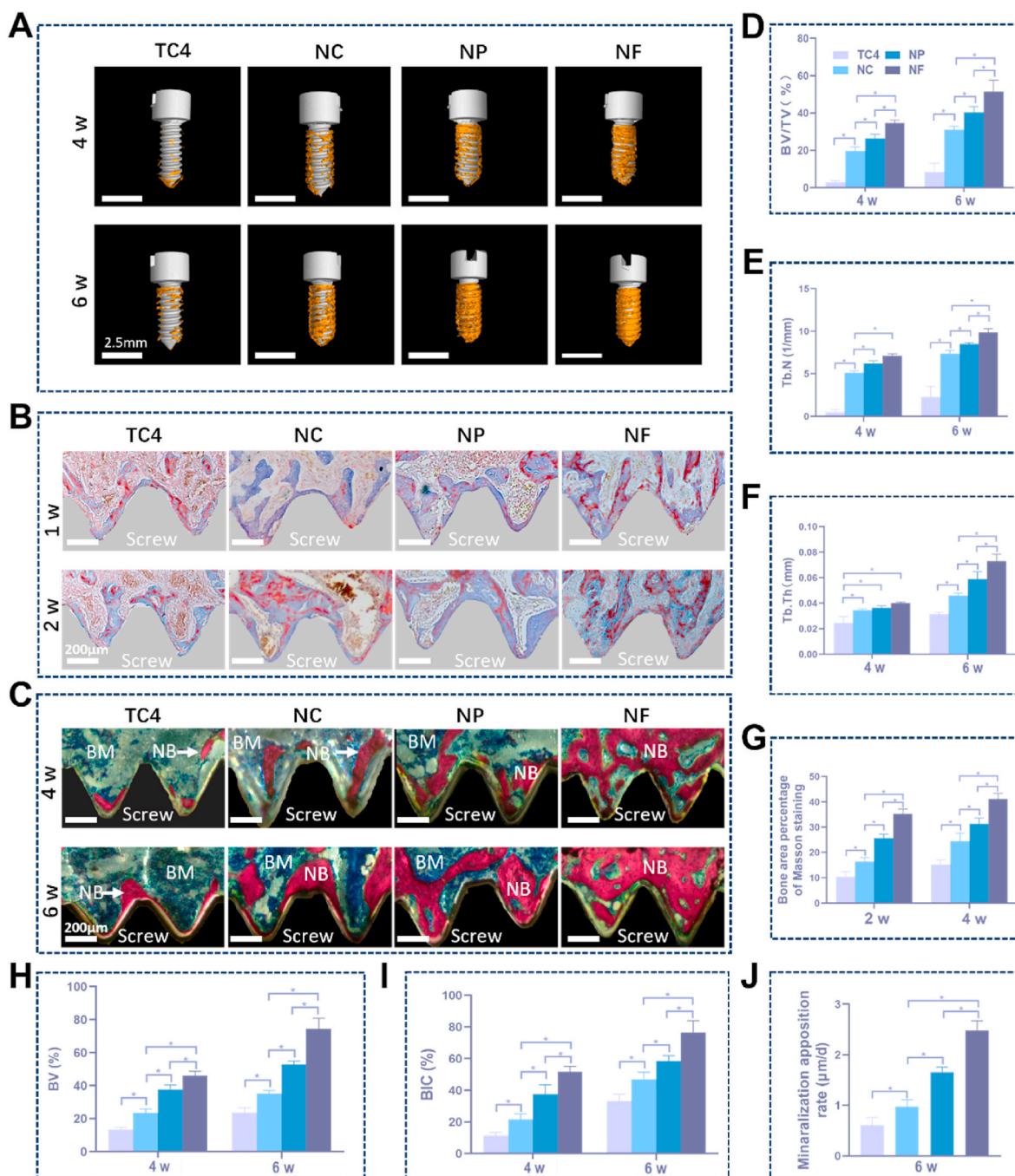


**Fig. 8.** Osteointegration around bare and nano-CeO<sub>2-x</sub> coated TC4 screws implanted in rat femoral condyles at 1, 2, 4 and 6 w: (A) Micro-CT reconstructed images of the newly formed bone (yellow) around screws (white); (B) Masson and (C) VG-stained images (NB: new bone; BM: bone marrow) of the new bone adjacent to screw. (D) Quantitative ratio of new bone volume to total area around the reconstructed screw (BV/TV, %), (E) number of trabeculae (Tb. N, 1/mm), (F) bone trabecular thickness (Tb. Th, 1/mm) calculated from Micro-CT reconstructed images. (G) Bone area percentage of Masson staining. (H) Quantified percentage of new bone volumes (BV, %) as well as (I) bone-implant contact ratios (BIC, %) calculated from the VG staining images. \**p* < 0.05.

coated TC4 (in particular NF) exhibited statistically higher MAR values than bare TC4 (Fig. 8J).

#### 4. Conclusions

Herein, nano-shaped (NC, NP and NF) cerium dioxide (CeO<sub>2-x</sub>) coatings equivalent to nanozyme for multiple free radical scavenging were prepared on titanium alloy (TC4) surfaces by hydrothermal treatment method. Nano-CeO<sub>2-x</sub> coatings (especially NF) for ROS and NO scavenging thereby induced M2-polarized macrophages conducive to

osteoinnervation modulation and vascularized osseointegration. The obvious revascularization and bone formation acted by Nano-CeO<sub>2-x</sub> coatings (in specific NF) in DSS and CM patterns *in vitro*, were perceived and the latter mode exhibited prominent enhance due to M2-macrophage secreted anti-inflammatory cytokines and growth factors. Inflammation, angiogenesis and osteogenesis in tissue around nano-CeO<sub>2-x</sub> coated TC4 screws in rat femoral condyles further confirmed that NF displayed osteoinnervation and osseointegration functions. The underlying mechanism was that NF inhibited macrophage PI3K-AKT signaling pathway playing a key role in macrophage polarization. In

summary, nano-CeO<sub>2-x</sub> coatings for multiple free radical scavenging contributed to immunomodulation and subsequent osseointegration, providing a promising insight into for surface structural and chemical design of orthopedic implants.

### Ethics approval and consent to participate

Surgical procedures on experimental animals were approved by the Institutional Laboratory Animal Centre and the Ethics Committee of the Fourth Military Medical University.

### CRedit authorship contribution statement

**Shusen Bao:** Writing – original draft, Investigation, Data curation. **Dongmei Yu:** Writing – original draft, Methodology, Formal analysis, Data curation. **Zhen Tang:** Software, Data curation. **Hao Wu:** Validation, Supervision, Methodology. **Hao Zhang:** Validation, Software. **Ning Wang:** Resources, Methodology. **Yichao Liu:** Software. **Hai Huang:** Supervision. **Chaozong Liu:** Writing – review & editing, Supervision. **Xiaokang Li:** Writing – review & editing, Supervision, Resources. **Zheng Guo:** Writing – review & editing, Supervision, Funding acquisition, Conceptualization.

### Declaration of competing interest

The authors disclaim any known financial interests or personal relationships that might influence the work reported in this paper.

### Acknowledgements

This study was supported by grants from the National Key Research and Development Program of China (grant number 2017YFC1104900) and the National Natural Science Foundation of China (No. 82372124, 51871239, and 51771227). The authors also acknowledge the support from the Incubation Program of China Army Medical Science and Technology Youth Training Program (No. 17QNP021) and the Everest Program of Air Force Military Medical University (No. 2020ZFC002). Thanks to Ms. Yanhua Wen from the Institute of Bone Tumor, Tangdu Hospital, Air Force Military Medical University, for providing technical guidance. Appreciation for Researchers ([www.home-for-researchers.com](http://www.home-for-researchers.com)) help with schematic mapping. We appreciate Centre for Advancing Materials Performance from the Nanoscale (CAMP-Nano) for some material characterization test.

### Appendix A. Supplementary data

Supplementary data to this article can be found online at <https://doi.org/10.1016/j.bioactmat.2023.12.006>.

### References

- J.N. Katz, K.R. Arant, R.F. Loeser, Diagnosis and treatment of hip and knee osteoarthritis: a review, *JAMA* 325 (6) (2021) 568–578.
- M.L. Barnett, et al., Two-year evaluation of mandatory bundled payments for Joint replacement, *N. Engl. J. Med.* 380 (3) (2019) 252–262.
- R.J. Ferguson, et al., Hip replacement, *Lancet* 392 (10158) (2018) 1662–1671.
- National Joint Registry, National Joint Registry for England, Wales, Northern Ireland and the Isle of Man: 15th Annual Report, 2018. <http://www.njrreports.org.uk/>. (Accessed 1 October 2018).
- Agency for Healthcare Research and Quality, USA, HCUPnet:2014 National Procedures for ICD-9-CM Principal Procedure Code81, vol. 51, 2017. <https://hcupnet.ahrq.gov/#setup>. (Accessed 1 October 2018).
- M. Sundfeldt, et al., Aseptic loosening, not only a question of wear: a review of different theories, *Acta Orthop.* 77 (2) (2006) 177–197.
- A.P. Kusumbe, S.K. Ramasamy, R.H. Adams, Coupling of angiogenesis and osteogenesis by a specific vessel subtype in bone, *Nature* 507 (7492) (2014) 323–328.
- J. Raphael, et al., Multifunctional coatings to simultaneously promote osseointegration and prevent infection of orthopaedic implants, *Biomaterials* 84 (2016) 301–314.
- Z. Chen, T. Klein, R.Z. Murray, R. Crawford, J. Chang, C. Wu, et al., Osteoimmunomodulation for the development of advanced bone biomaterials, *Mater. Today* 19 (2016) 304–321.
- S. Franz, et al., Immune responses to implants - a review of the implications for the design of immunomodulatory biomaterials, *Biomaterials* 32 (28) (2011) 6692–6709.
- M. Li, et al., Tuning the surface potential to reprogram immune microenvironment for bone regeneration, *Biomaterials* 282 (2022), 121408.
- A. Shapouri-Moghaddam, et al., Macrophage plasticity, polarization, and function in health and disease, *J. Cell. Physiol.* 233 (9) (2018) 6425–6440.
- S.C. Funes, et al., Implications of macrophage polarization in autoimmunity, *Immunology* 154 (2) (2018) 186–195.
- X. Li, et al., ROS-responsive hydrogel coating modified titanium promotes vascularization and osteointegration of bone defects by orchestrating immunomodulation, *Biomaterials* 287 (2022), 121683.
- S.S. Jin, et al., A biomimetic hierarchical nanointerface orchestrates macrophage polarization and mesenchymal stem cell recruitment to promote endogenous bone regeneration, *ACS Nano* 13 (6) (2019) 6581–6595.
- Y. Yang, et al., Development of a novel nitric oxide (NO) production inhibitor with potential therapeutic effect on chronic inflammation, *Eur. J. Med. Chem.* 193 (2020), 112216.
- G. Chen, C. Deng, Y.P. Li, TGF-beta and BMP signaling in osteoblast differentiation and bone formation, *Int. J. Biol. Sci.* 8 (2) (2012) 272–288.
- Y. Niu, et al., Modulating macrophage activities to promote endogenous bone regeneration: biological mechanisms and engineering approaches, *Bioact. Mater.* 6 (1) (2021) 244–261.
- S.S. Jin, et al., A biomimetic hierarchical nanointerface orchestrates macrophage polarization and mesenchymal stem cell recruitment to promote endogenous bone regeneration, *ACS Nano* 13 (6) (2019) 6581–6595.
- X. Zhou, et al., Multifunctional graphdiyne-cerium oxide nanozymes facilitate MicroRNA delivery and attenuate tumor hypoxia for highly efficient radiotherapy of esophageal cancer, *Adv. Mater.* 33 (24) (2021), e2100556.
- S. Ren, et al., Cerium oxide nanoparticles loaded nanofibrous membranes promote bone regeneration for periodontal tissue engineering, *Bioact. Mater.* 7 (2022) 242–253.
- Q.Z.W.D. Bo Li, Reshaping cardiac microenvironments by macrophage-derived extracellular vesicles-coated Pd@CeO<sub>2</sub> heterostructures for myocardial ischemia/reperfusion injury therapy, *Mater. Today* 65 (2023) 47–61.
- F. Muhammad, et al., Nanoceria as an electron reservoir: spontaneous deposition of metal nanoparticles on oxides and their anti-inflammatory activities, *ACS Nano* 16 (12) (2022) 20567–20576.
- J. Li, et al., Valence state manipulation of cerium oxide nanoparticles on a titanium surface for modulating cell fate and bone formation, *Adv. Sci.* 5 (2) (2018), 1700678.
- Y. Yu, et al., Cerium oxide nanozyme attenuates periodontal bone destruction by inhibiting the ROS-NFκB pathway, *Nanoscale* 14 (7) (2022) 2628–2637.
- F. Han, et al., Targeting endogenous reactive oxygen species removal and regulating regenerative microenvironment at annulus fibrosus defects promote tissue repair, *ACS Nano* 17 (8) (2023) 7645–7661.
- X. Li, et al., Surface treatments on titanium implants via nanostructured ceria for antibacterial and anti-inflammatory capabilities, *Acta Biomater.* 94 (2019) 627–643.
- J.M. Dowding, et al., Cerium oxide nanoparticles scavenge nitric oxide radical (NO), *Chem. Commun.* 48 (40) (2012) 4896–4898.
- P. Jiang, et al., Advanced surface engineering of titanium materials for biomedical applications: from static modification to dynamic responsive regulation, *Bioact. Mater.* 27 (2023) 15–57.
- Y. Wang, et al., Targeted therapy of atherosclerosis by a broad-spectrum reactive oxygen species scavenging nanoparticle with intrinsic anti-inflammatory activity, *ACS Nano* 12 (9) (2018) 8943–8960.
- Y. Yang, et al., Development of a novel nitric oxide (NO) production inhibitor with potential therapeutic effect on chronic inflammation, *Eur. J. Med. Chem.* 193 (2020), 112216.
- K. Kashfi, J. Kannikal, N. Nath, Macrophage reprogramming and cancer therapeutics: role of iNOS-derived NO, *Cells* 10 (11) (2021).
- Y.G. Kim, et al., Ceria-based therapeutic antioxidants for biomedical applications, *Adv. Mater.* (2023), e2210819.
- D.M. Yu, D.Y. S.G., Interrod spacing dependent angiogenesis and osseointegration of Na<sub>2</sub>TiO<sub>3</sub> nanorods-patterned arrays via immunoregulation, *Chem. Eng. J.* 426 (2021) 131187–131201.
- S.L. Ellis, et al., The relationship between bone, hemopoietic stem cells, and vasculature, *Blood* 118 (6) (2011) 1516–1524.
- S. Chigurupati, et al., Effects of cerium oxide nanoparticles on the growth of keratinocytes, fibroblasts and vascular endothelial cells in cutaneous wound healing, *Biomaterials* 34 (9) (2013) 2194–2201.
- D. Yu, et al., Cubic multi-ions-doped Na<sub>2</sub>TiO<sub>3</sub> nanorod-like coatings: structure-stable, highly efficient platform for ions-exchanged release to immunomodulatory promotion on vascularized bone apposition, *Bioact. Mater.* 18 (2022) 72–90.
- M. Zhang, et al., The effects of platelet-derived growth factor-BB on bone marrow stromal cell-mediated vascularized bone regeneration, *Stem Cell. Int.* (2018), 3272098, 2018.
- P. Qiu, et al., Periosteal matrix-derived hydrogel promotes bone repair through an early immune regulation coupled with enhanced angio- and osteogenesis, *Biomaterials* 227 (2020), 119552.

- [40] S. Stegen, N. van Gestel, G. Carmeliet, Bringing new life to damaged bone: the importance of angiogenesis in bone repair and regeneration, *Bone* 70 (2015) 19–27.
- [41] Z. Xu, et al., Type H blood vessels in coupling angiogenesis-osteogenesis and its application in bone tissue engineering, *J. Biomed. Mater. Res. B Appl. Biomater.* 111 (7) (2023) 1434–1446.
- [42] H. Xie, et al., PDGF-BB secreted by preosteoclasts induces angiogenesis during coupling with osteogenesis, *Nat. Med.* 20 (11) (2014) 1270–1278.
- [43] J. Yan, et al., Nintedanib ameliorates osteoarthritis in mice by inhibiting synovial inflammation and fibrosis caused by M1 polarization of synovial macrophages via the MAPK/PI3K-AKT pathway, *FASEB J.* 37 (10) (2023), e23177.
- [44] C. Zhao, et al., Loss of PTEN expression is associated with PI3K pathway-dependent metabolic reprogramming in hepatocellular carcinoma, *Cell Commun. Signal.* 18 (1) (2020) 131.